COMPUTATION OF TURBULENT FLOW IN A SQUARE DUCT: ASPECTS OF THE SECONDARY FLOW AND ITS ORIGIN

F. M. WANG,† Y. T. CHEW, B. C. KHOO and K. S. YEO

Mechanical & Production Engineering Department, National University of Singapore,
Kent Ridge, Singapore 0511

Abstract—A numerical study of turbulent flow in a straight duct of square cross-section is made. An order-of-magnitude analysis of the 3-D, time-averaged Navier–Stokes equations resulted in a parabolic form of the Navier–Stokes equations. The governing equations, expressed in terms of a new vector-potential formulation, are expanded as a multi-deck structure with each deck characterized by its dominant physical forces. The resulting equations are solved using a finite-element approach with a bicubic element representation on each cross-sectional plane. The numerical integration along the streamwise direction is carried out with finite-difference approximations until a fully-developed state is reached. The computed results agree well with other numerical studies and compare very favorably with the available experimental data. One important outcome of the current investigation is the interpretation analytically that the driving force of the secondary flow in a square duct comes mainly from the second-order terms of the difference in the gradients of the normal and transverse Reynolds stresses in the axial vorticity equation.

NOMENCLATURE

C_1 = Empirical value of 1.5 from Ref. [16] for turbulence modeling, equations (5)
C_μ = Value of 0.090 for k–ϵ modeling, equations (8)
$C_{\epsilon 1}$ = Value of 1.44 for k–ϵ modeling, equations (8)
$C_{\epsilon 2}$ = Value of 1.92 for k–ϵ modeling, equations (8)
C_f = Dimensionless skin friction coefficient, $2\bar{\tau}_w/\rho U_b^2$
D_h = Hydraulic diameter of the square duct
k = Non-dimensional turbulence kinetic energy
L_1 = Streamwise length scale (duct length) for non-dimensionalizing purposes, $O(L_2/L_1) = \delta$
$L_2 \equiv D_h$, Transverse streamwise length scale for non-dimensionalizing purposes
L' = Turbulent characteristic length for non-dimensionalizing purposes, $(L'/L_2) = \delta^{1/2}$
$\bar{p}$ = Mean pressure, non-dimensionalized w.r.t. ρU^{*2}
P_0 = Production of turbulence kinetic energy, equation (28)
$Re \equiv U^* D_h/v$, Reynolds number
U_b = Bulk streamwise velocity
U_{1max} = Maximum streamwise velocity
U_1 = Mean streamwise velocity, non-dimensionalized w.r.t. U^*
U_2, U_3 = Mean transverse velocity, non-dimensionalized w.r.t. V^*
u_i = Fluctuation velocity component in the i direction
u_{ij} = Reynolds stresses non-dimensionalized w.r.t. $(V')^2$
U^* = Streamwise velocity scale for non-dimensionalizing purposes, $U^* \equiv U_b$

U_τ = Shear velocity at the wall, $(\bar{\tau}_w/\rho)^{1/2}$
V^* = Transverse velocity scale for non-dimensionalizing purposes, $(V^*/U^*) = \delta$
$(V')^2$ = Turbulent characteristic energy scale for non-dimensionalizing Reynolds stresses, k and ϵ, $(V'/U^*)^2 = \delta$
x_1 = Streamwise coordinate, non-dimensionalized w.r.t. L_1
x_2, x_3 = Transverse coordinate, non-dimensionalized w.r.t. L_2

Superscripts

$'$ = Dimensional quantity.

Greek symbols

α = Empirical value of 0.7636 from Ref. [16] for turbulence modeling, equations (5)
β = Empirical value of 0.1041 from Ref. [16] for turbulence modeling, equations (5)
γ = Empirical value of 0.182 from Ref. [16] for turbulence modeling, equations (5)
σ_ϵ = Value of 1.3 for k–ϵ modeling, equations (8)
σ_k = Value of 1.0 for k–ϵ modeling, equations (8)
ϵ = Non-dimensional turbulence dissipation
$\delta \equiv 1/Re^{1/2}$, a small parameter
ρ = Density
v = Kinematic viscosity
μ_t = Non-dimensional turbulent viscosity, equations (23) and (24)
Ω = Dimensionless vorticity, equation (34)
ψ = A stream function, equation (32) or (34)
ϕ = A potential scalar function, equation (31) or (33)

1. INTRODUCTION

Turbulent flows of non-circular cross-section are found in many engineering applications such as heat exchangers, ventilation, air-conditioning systems and air-intake ducts of jet engines. An

---

†Permanent address: Institute of Mechanics, Academia Sinica, Beijing 100080, People's Republic of China.

important physical aspect of these flows is the presence of secondary motions in the plane perpendicular to the streamwise direction. Unlike laminar flow or flow in a curved duct, where the secondary motion is pressure-induced or due to the action of centrifugal forces (sometimes referred to as Prandtl's first kind), the secondary motion of the turbulent flow through a straight duct is driven purely by turbulent stresses (commonly referred to as Prandtl's second kind). Although the velocity of this secondary motion is only of the order of 2–3% of the bulk streamwise velocity, its very presence has far-reaching consequences. It causes bulging of the velocity contours towards the corners, hence affecting sediment transport and heat transfer characteristics in the flow.

A considerable number of experimental investigations have been carried out on turbulent flow in straight ducts. Nikuradse [1] was perhaps the first to observe the secondary motion in non-circular ducts using flow visualization. Hoagland [2] reported the first measurements of the secondary motion. Subsequent measurements have also been reported by Brundett and Baines [3], Gessner and Jones [4], Launder and Ying [5] and Gessner and Emery [6], among others, for flow in a square duct. Flow in a triangular duct has been investigated by Aly *et al.* [7].

The first calculation of secondary flow in straight non-circular ducts was carried out by Launder and Ying [5]. The turbulent closure model suggested by these authors, or extended variations of this model, have since been used by a number of authors to predict a fairly wide range of flows [6, 8, 9]. Most of these calculations adopted the strategy outlined by Patankar and Spalding [10] and found in the algorithm called SIMPLE.

In our work, an order-of-magnitude analysis of the time-averaged governing momentum equations gives rise to the parabolized Navier–Stokes equations (Sections 2.1 and 2.2). Together with the formulation of the potential stream function and velocity potential (Section 2.3) for the description of the streamwise vorticity and the streamwise velocity, respectively, we have a system of four parabolic equations and two Poisson equations. This compares favorably with the other numerical studies, notably Demuren and Rodi [11], whose scheme involves five parabolic and two Poisson equations.

Our system of equations is then described in a multi-region framework on a plane perpendicular to the streamwise direction, so as to reflect the local balance of the *dominant* physical forces in each region (Section 3). The idea is very similar to that carried out in analytical work using triple-deck expansion to elucidate better the physics of the flow. As shown subsequently, this expansion enables us to depict clearly the origin of the secondary motion in a square-duct section flow, which is unlike other schemes offering complete simulation of all the governing terms. In the present turbulence modeling, starting from the algebraic Reynolds stress equation adopted from Demuren and Rodi [11], the stress components are solved using the Chen and Patel [12] two-layer approach proposed for modeling of eddy viscosity relations, which are assumed valid for the primary shear stress and other terms. This is different from the approach used by Demuren and Rodi where the eddy viscosity based on the k–ϵ model is used throughout. In our application, the no-slip boundary condition at the wall is used directly in place of the common wall function approach, since the regions close to the wall and the corner are known to influence greatly the characteristics of secondary flow. This is also the stand taken by Myong and Kobayashi [13–15], who are concerned about the undue influence of wall treatment on the generation of secondary flow; and hence they used an anisotropic, low Reynolds number (Re) k–ϵ turbulence model with no-slip conditions at the wall. In the latter's work, it is further shown that the commonly adopted wall function approach of specifying the variables along the first grid point next to the wall in the logarithmic regime, usually taken from 2-D flow, is not completely valid for 3-D flow. The importance of ensuring correct boundary conditions and their consequential influence on secondary flow near the wall/corner cannot be overstated. The work of Myong and Kobayashi also clearly illustrates the successful implementation of an anisotropic k–ϵ turbulence model for predicting the complex secondary flow in a square duct.

In our implementation, the numerical integration in the cross-plane is based on a bicubic, finite-element method with C^1 continuity at the element interfaces, which ensures continuity of the gradient across the boundaries of the multi-region (Section 4). The use of the finite element method implies that future study of different cross-sectional shapes can be easily implemented. For the streamwise direction, a finite-difference marching procedure is employed. Combination of both finite-element and finite-difference schemes can also greatly facilitate other future numerical work
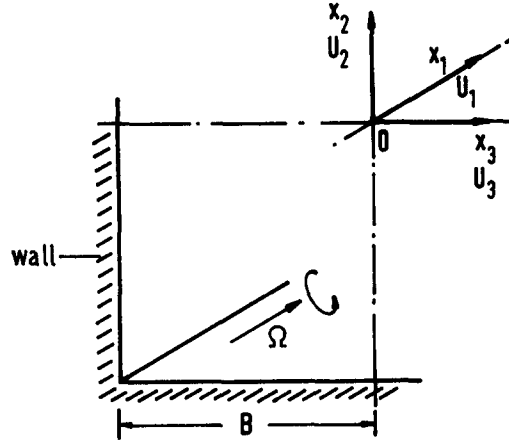
Fig. 1. Coordinate system with the origin 0 set at the center of the square duct; Ω is the axial vorticity.

on flow through varying cross-sectional shapes in the streamwise direction. Such flow is often encountered in turbomachines, where the intake section and the rotary portion of machines are different. As will be shown subsequently (Section 5), the present computed results on flow in a straight square duct compare very favorably with the available experimental data, and other numerical works.

2. MATHEMATICAL MODEL

2.1. Governing equations

The steady-state, time-averaged 3-D Navier–Stokes equations, in Cartesian tensor notation (see Fig. 1), may be expressed as follows:

the continuity equation,

$$\frac{dU_i'}{dx_i'} = 0; \tag{1}$$

the streamwise momentum equation,

$$U_j'\frac{\partial U_1'}{\partial x_j'} = -\frac{1}{\rho}\frac{\overline{dP'}}{dx_1'} - \frac{\partial \overline{u_1' u_j'}}{\partial x_j'} + \nu\frac{\partial^2 U_1'}{\partial x_j' \partial x_j'}; \tag{2}$$

and

the momentum equations governing the secondary velocities U_2' and U_3',

$$U_j'\frac{\partial U_j'}{\partial x_j'} = -\frac{1}{\rho}\frac{\partial P'}{\partial x_L'} - \frac{\partial \overline{u_L' u_j'}}{\partial x_j'} + \nu\frac{\partial^2 U_L'}{\partial x_j' \partial x_j'} \quad (L = 2, 3). \tag{3}$$

Here the superscript prime refers to a dimensional quantity, U_j' is the component of the mean velocity vector in the x_j-direction ($j = 1, 2, 3$), ρ is the density and ν is the fluid kinematic viscosity. Note that the gradient $\partial P'/\partial x_1'$ originally appearing in equation (2) has been replaced by the cross-sectional average pressure gradient $\overline{\partial P'/\partial x_1'}$.

The Reynolds stress components $\overline{u_i' u_j'}$ in the following governing equation are derived by Demuren and Rodi [11] from the modeled transport equation given by Launder et al. [16] and the assumption of local equilibrium (i.e. convection and diffusion effects are neglected):

$$(1-\alpha)\left(-\overline{u_i' u_L'}\frac{\partial U_j'}{\partial x_L'} - \overline{u_j' u_L'}\frac{\partial U_i'}{\partial x_L'}\right) + \beta\left(\overline{u_i' u_L'}\frac{\partial U_L'}{\partial x_j'} + \overline{u_j' u_L'}\frac{\partial U_L'}{\partial x_i'}\right)$$

$$-\gamma k'\left(\frac{dU_i'}{dx_j'} + \frac{dU_j'}{dx_i'}\right) - \frac{\epsilon'}{k'}\left[C_1\overline{u_i' u_j'} + \tfrac{2}{3}(1 - \alpha - \beta - C_1)\delta_{ij}k'\right] = 0, \tag{4}$$

where the various symbols take on the usual meanings and the empirical parameters are defined as:

$$C_1 = 1.5, \quad \alpha = 0.7636, \quad \beta = 0.1091, \quad \gamma = 0.182. \tag{5}$$

Following Demuren and Rodi [11], equation (4) is solved for the various stress components [see equations (17)–(22)] with similar simplification of some terms and adoption of an eddy viscosity relation, especially for the primary shear stresses. (The interested reader is referred to the original work of Demuren and Rodi [11] for details.) However, instead of expressing the eddy viscosity solely by the isotropic k–ϵ model as in the former, we used the two-layer approach of Chen and Patel [12]. In the region away from the wall, the turbulent eddy viscosity μ_t' is related to the turbulent kinetic energy k', and its rate of dissipation ϵ', by

$$\mu_t' = C_\mu \frac{k'^2}{\epsilon'} \tag{6}$$

and k' and ϵ' are calculated from

$$U_j' \frac{\partial k'}{\partial x_j'} = \frac{\partial}{\partial x_j'}\left[\left(\frac{1}{\sigma_k}\mu_t' + v\right)\frac{\partial k'}{\partial x_j'}\right] + P_k' - \epsilon' \tag{7a}$$

and

$$U_j' \frac{\partial \epsilon'}{\partial x_j'} = \frac{\partial}{\partial x_j'}\left[\left(\frac{1}{\sigma_\epsilon}\mu_t' + v\right)\frac{\partial \epsilon'}{\partial x_j'}\right] + \frac{\epsilon'}{k'}[C_{\epsilon1}P_k' - C_{\epsilon2}\epsilon']. \tag{7b}$$

Here $P_k' = -\overline{u_i'u_k'}(\partial U_i'/\partial x_k')$ is the production of turbulent kinetic energy. In equations (7a,b), $i, j, k = 1, 2, 3$ and C_μ, σ_k, σ_ϵ, $C_{\epsilon1}$ and $C_{\epsilon2}$ are empirical constants, which have been assigned to standard values:

$$C_\mu = 0.090, \quad \sigma_k = 1.0, \quad \sigma_\epsilon = 1.3, \quad C_{\epsilon1} = 1.44, \quad C_{\epsilon2} = 1.92. \tag{8}$$

In the region close to the wall, the turbulent viscosity and rate of energy dissipation are expressed in terms of turbulent kinetic energy and specified length scales, i.e.

$$\mu_t' = C_\mu\sqrt{k'}\, l_\mu', \quad \epsilon' = k'^{3/2}/l_\epsilon', \tag{9}$$

where $l_\mu' = C_L y[1 - \exp(-R_y'/70)]$, $l_\epsilon' = C_L y[1 - \exp(-R_y'/2C_L)]$, $C_L = \kappa C_\mu^{-3/4}$, $R_y' = R\sqrt{k'}\, y$ and $\kappa = 0.418$. Here y is the distance away from the wall. In the corner region, y is the minimum of the two distances from the walls. The turbulent kinetic energy is determined from equation (7a).

2.2. Dimensional analysis

In this section we derive a set of parabolic Navier–Stokes equations from equations (1)–(3). The following assumptions are made:

(1) The transverse mean velocities and transverse pressure variations are much smaller than the axial velocity and axial pressure gradient, respectively.
(2) The flow is characterized by the predominant streamwise flow direction, along which there is no flow reversal.
(3) The diffusive transport process in the streamwise direction is neglected.
(4) The streamwise elliptic characteristic of the Navier–Stokes equation is enforced only through the adoption of a suitable mean pressure field $\partial P'/\partial x_i'$ [10].

For non-dimensionalization, we select U^* and V^* as the streamwise and transverse velocity component scales, respectively. The corresponding length scales for non-dimensionalization are denoted by L_1 and L_2. The turbulent characteristic length and energy scales are denoted by L' and V'^2. With these, we define

$$U_1 = \frac{U_1'}{U^*}, \quad U_L = \frac{U_L'}{V^*}, \quad x_1 = \frac{x_1'}{L_1}, \quad x_L = \frac{x_L'}{L_2}, \quad u_{ij} = \frac{\overline{u_i'u_j'}}{V'^2}R_{ij}, \quad \bar{P}(x_1) + \delta P(x_L) = \frac{P'}{\rho U^{*2}} \quad (L = 2, 3), \tag{10}$$

where $R_{ij} = \overline{u_i'u_j'}(\overline{u_i'u_i'}\,\overline{u_j'u_j'})^{-1/2}$ are the correlation coefficients of the turbulent velocities. Based on the experiments that the secondary velocities are $O(2-3\%)$ of the primary bulk velocity, we set $\delta = O(1/\mathrm{Re}^{1/2})$ as a small parameter, where

$$\mathrm{Re} = \frac{U^*D_h}{v}, \quad O\left(\frac{V^*}{U^*}\right) = O\left(\frac{L_2}{L_1}\right) = O\left(\frac{V'^2}{U^{*2}}\right) = \delta, \quad R_{ij} = O(1). \tag{11}$$

We note here that $D_h(=L_2)$ is the hydraulic diameter, L_1 is the length of the duct and $U_b(=U^*)$ is the bulk velocity. [In subsequent implementations of the numerics, δ is set equal to $1/\mathrm{Re}^{1/2}$ and all the relations expressed in equations (11) are taken to be exact.] The non-dimensional forms of the governing equations (1)–(3) can then be written as:

$$\frac{\partial U_i}{\partial x_i} = 0, \tag{12}$$

$$U_i \frac{\partial U_1}{\partial x_i} = -\frac{\overline{dP}}{dx_1} - \frac{\partial u_{1L}}{\partial x_L} + \frac{1}{\mathrm{Re}} \left(\frac{L_1}{L_2} \frac{\partial^2}{\partial x_L \partial x_L} \right) U_1, \tag{13}$$

$$\delta U_i \frac{\partial U_2}{\partial x_i} = -\frac{\partial P}{\partial x_2} - \delta \frac{\partial u_{12}}{\partial x_1} - \frac{\partial u_{2L}}{\partial x_L} + \delta \frac{1}{\mathrm{Re}} \left(\frac{L_1}{L_2} \frac{\partial^2}{\partial x_L \partial x_L} \right) U_2 \tag{14}$$

and

$$\delta U_i \frac{\partial U_3}{\partial x_i} = -\frac{\partial P}{\partial x_3} - \delta \frac{\partial u_{13}}{\partial x_1} - \frac{\partial u_{3L}}{\partial x_L} + \delta \frac{1}{\mathrm{Re}} \left(\frac{L_1}{L_2} \frac{\partial^2}{\partial x_L \partial x_L} \right) U_3. \tag{15}$$

Here $i = 1, 2, 3$, $L = 2, 3$.

In the momentum equations, u_{ij} must necessarily be $O(\delta)$. It follows that $\partial u_{11}/\partial x_1$ is of higher order and is neglected in equation (13). For equations (14) and (15), the pressure variation in the respective transverse directions must balance the convective and Reynolds stress terms to order $O(\delta)$. The diffusion terms in the streamwise direction are of order $O(\delta^2)$ and neglected in equations (13)–(15).

Next, on defining

$$k = \frac{k'}{V'^2}, \quad \epsilon = \frac{\epsilon' L'}{V'^3} \tag{16}$$

and noting that $O(u_{ij}) \simeq O(\delta)$, $O(k) \simeq O(\delta)$, $O(C_\mu/\epsilon) \simeq O(C_\mu \beta/C_1 \epsilon) \simeq O(1)$ and $O(L'/L_2) = \delta^{1/2}$, the six components of the Reynolds stress tensor can then be expressed as follows on the basis of equation (4) [we retain only these terms whose order is required for compatibility with equations (13)–(15)]:

$$u_{11} = \frac{2}{3C_1}(\alpha + \beta + C_1 - 1)k - \frac{2}{3C_1} C_\mu \frac{k^3}{\epsilon^2}(1 - \alpha) \left[\left(\frac{\partial U_1}{\partial x_2} \right)^2 + \left(\frac{\partial U_1}{\partial x_3} \right)^2 \right], \tag{17}$$

$$u_{22} = \frac{2}{3C_1}(\alpha + \beta + C_1 - 1)k - \frac{2}{C_1} \mu_t \frac{k}{\epsilon} \beta \left[\left(\frac{\partial U_1}{\partial x_2} \right)^2 \right] - 2\delta \mu_t \left[\frac{\partial U_2}{\partial x_2} \right], \tag{18}$$

$$u_{33} = \frac{2}{3C_1}(\alpha + \beta + C_1 - 1)k - \frac{2}{C_1} \mu_t \frac{k}{\epsilon} \beta \left[\left(\frac{\partial U_1}{\partial x_3} \right)^2 \right] - 2\delta \mu_t \left[\frac{\partial U_3}{\partial x_3} \right], \tag{19}$$

$$u_{12} = -\mu_t \left[\frac{\partial U_1}{\partial x_2} \right], \tag{20}$$

$$u_{13} = -\mu_t \left[\frac{\partial U_1}{\partial x_3} \right] \tag{21}$$

and

$$u_{23} = -\frac{2}{C_1} \mu_t \frac{k}{\epsilon} \beta \left[\left(\frac{\partial U_1}{\partial x_2} \frac{\partial U_1}{\partial x_3} \right) \right] - 2\delta \mu_t \left[\frac{\partial U_2}{\partial x_3} + \frac{\partial U_3}{\partial x_2} \right]. \tag{22}$$

μ_t is given by the non-dimensional form of equations (6) and (9) for application to the region far away and near the walls, respectively. They are expressed as

$$\mu_t = C_\mu \frac{k^2}{\epsilon} \tag{23}$$

and

$$\mu_t = C_\mu \sqrt{k} \, l_\mu. \tag{24}$$

The dimensionless turbulent kinetic energy k is evaluated from the equation

$$U_i \frac{\partial k}{\partial x_i} = \frac{L_1}{L_2} \frac{\partial}{\partial x_L} \left[\left(\frac{1}{\sigma_k} C_\mu \frac{k^2}{\epsilon} + \frac{1}{\text{Re}} \right) \frac{\partial k}{\partial x_L} \right] + \frac{L_1}{L_2} [P_0 - \epsilon], \tag{25}$$

while the dissipation term ϵ is governed by the expression

$$U_i \frac{\partial \epsilon}{\partial x_i} = \frac{L_1}{L_2} \frac{\partial}{\partial x_L} \left[\left(\frac{1}{\sigma_\epsilon} C_\mu \frac{k^2}{\epsilon} + \frac{1}{\text{Re}} \right) \frac{\partial \epsilon}{\partial x_L} \right] + \frac{L_1}{L_2} \frac{\epsilon}{k} [C_{c1} P_0 - C_{c2} \epsilon] \tag{26}$$

for the region far away from the walls. In the near-wall regions, we take

$$\epsilon = k^{3/2}/l_c. \tag{27}$$

For all the above equations (23)–(27)

$$P_0 = -u_{1L} \frac{\partial U_L}{\partial x_L} - \delta \left(u_{11} \frac{\partial U_1}{\partial x_1} + u_{jL} \frac{\partial U_j}{\partial x_L} \right) \quad (j, L = 2, 3); \tag{28}$$

$$l_\mu = C_L x_L [1 - \exp(-R_x/70)], \quad l_c = C_L x_L [1 - \exp(-R_x/2C_L)], \quad R_x = R\sqrt{k}\, x_L, \quad C_L = \kappa C_\mu^{-3/4}.$$

2.3. A vector-potential function formulation

The parabolic properties of the governing equations with a suitable pressure-gradient algorithm [10] permit us to employ a special vector-potential function formulation in which only the streamwise component of the vorticity tensor needs to be taken into consideration. We may express

$$\mathbf{U} = U_1 \mathbf{I} + U_2 \mathbf{J} + U_3 \mathbf{K} = U_1 \mathbf{I} + \mathbf{V}_s, \tag{29}$$

where $\mathbf{I}$, $\mathbf{J}$, $\mathbf{K}$ are the unit vectors along the x_1, x_2 and x_3 directions, respectively, and $\mathbf{V}_s$ is a sum of vectors in the transverse plane,

$$\mathbf{V}_s = \mathbf{I}_n + \mathbf{S}_o = (I_{n2} + S_{o2}) \mathbf{J} + (I_{n3} + S_{o3}) \mathbf{K}. \tag{30}$$

Here the vector $\mathbf{V}_s$, is decomposed into its irrotational and solenoidal components denoted by $\mathbf{I}_n$ and $\mathbf{S}_o$, respectively, while I_{n2}, S_{o2}, I_{n3} and S_{o3} represent their components along the x_2 and x_3 directions, as indicated by the respective subscripts. $\mathbf{I}_n$ can be defined by a potential scalar function ϕ as

$$\mathbf{I}_n = \text{Grad } \phi, \quad \text{i.e.} \quad I_{n2} = \frac{\partial \phi}{\partial x_2}, \quad I_{n3} = \frac{\partial \phi}{\partial x_3}. \tag{31}$$

Another scalar ψ (which can be considered as one component of a vector potential stream function $\boldsymbol{\Psi}$), is introduced by using the divergence-free condition of $\mathbf{S}_o$, such that

$$S_{o2} = \frac{\partial \psi}{\partial x_3}, \quad S_{o3} = -\frac{\partial \psi}{\partial x_2}. \tag{32}$$

Taking the divergence of equation (29), ϕ is found to satisfy

$$\frac{\partial^2 \phi}{\partial x_2 \partial x_2} + \frac{\partial^2 \phi}{\partial x_3 \partial x_3} = -\frac{\partial U_1}{\partial x_1}. \tag{33}$$

Furthermore, the streamwise component of the vorticity tensor is related to ψ through

$$\frac{\partial^2 \psi}{\partial x_2 \partial x_2} + \frac{\partial^2 \psi}{\partial x_3 \partial x_3} = \Omega, \quad \text{where } \Omega = \frac{\partial U_2}{\partial x_3} - \frac{\partial U_3}{\partial x_2}. \tag{34}$$

With the above, the four mean-flow equations (12)–(15) can be reduced to the following two equations:

$$U_i \frac{\partial U_1}{\partial x_i} = -\frac{\overline{dP}}{dx_1} - \frac{\partial u_{1L}}{\partial x_L} + \frac{1}{\text{Re}} \left[\frac{L_1}{L_2} \frac{\partial^2}{\partial x_L \partial x_L} \right] U_1 \tag{35}$$

and

$$\delta U_i \frac{\partial \Omega}{\partial x_i} = \delta \left\{ \frac{\partial U_1}{\partial x_1} \Omega - \frac{\partial U_2}{\partial x_1} \frac{\partial U_1}{\partial x_3} + \frac{\partial U_3}{\partial x_1} \frac{\partial U_1}{\partial x_2} + \frac{\partial}{\partial x_1} \left[\frac{\partial u_{13}}{\partial x_2} - \frac{\partial u_{12}}{\partial x_3} \right] \right\} + \frac{\partial^2}{\partial x_2 \partial x_3} (u_{33} - u_{22})$$

$$- \left(\frac{\partial^2}{\partial x_3 \partial x_3} - \frac{\partial^2}{\partial x_2 \partial x_2} \right) u_{23} + \delta \frac{1}{Re} \left[\frac{L_1}{L_2} \frac{\partial^2}{\partial x_L \partial x_L} \right] \Omega \quad (36)$$

for $i = 1, 2, 3$; $L = 2, 3$. Here

$$U_2 = \frac{\partial \phi}{\partial x_2} + \frac{\partial \psi}{\partial x_3} \quad \text{and} \quad U_3 = \frac{\partial \phi}{\partial x_3} - \frac{\partial \psi}{\partial x_2}.$$

2.4. Origin of the secondary motion

In equation (36), the terms of order $O(\delta)$ represent a balance of higher order effects between the Reynolds stresses and the axial vorticity. In order to explain the possible origin of the secondary motion, we consider only the case of fully-developed flow. We expand u_{mn}, $m, n = 2, 3$, as a power series of δ:

$$u_{mn} = u_{mn0} + \delta u_{mn1} + \cdots. \quad (37)$$

The expansion in powers of δ enables equation (36) to be decomposed into different orders of magnitude:

$$O(1), \quad \frac{\partial^2}{\partial x_2 \partial x_3} (u_{330} - u_{220}) - \left(\frac{\partial^2}{\partial x_3 \partial x_3} - \frac{\partial^2}{\partial x_2 \partial x_2} \right) u_{230} = 0; \quad (38)$$

and

$$O(\delta), \quad U_i \frac{\partial \Omega}{\partial x_i} - \frac{1}{Re} \left[\frac{L_1}{L_2} \frac{\partial^2}{\partial x_L \partial x_L} \right] \Omega = \frac{\partial^2}{\partial x_2 \partial x_3} (u_{331} - u_{221}) - \left(\frac{\partial^2}{\partial x_3 \partial x_3} - \frac{\partial^2}{\partial x_2 \partial x_2} \right) u_{231}. \quad (39)$$

Equation (28) expresses the fact that at leading order, the terms representing the gradients of the normal and transverse Reynolds stresses balance each other, resulting in the production of zero axial vorticity. The convection and diffusion of axial vorticity are of secondary order, and are driven by the second-order gradient of the normal and transverse Reynolds stresses. These equations clearly demonstrate that the difference between the second-order gradient of the normal and transverse Reynolds stresses is the major source for generation of the secondary motion. This conclusion is further verified in Section 5, which describes the computations carried out to compare the magnitude of the second-order terms depicted in equation (39) and the total term corresponding to equation (36).

3. MULTIPLE STRUCTURE

The turbulence in duct flows (as well as in channel and boundary layer flows) is not only convected along the streamwise direction but also diffuses in the transverse direction; a result of the complex interaction between the effects of the kinematic viscosity and turbulent kinetic stresses. An outcome of this interaction is the presence of a multi-deck structure, wherein each deck is characterized by a balance of its dominant physical forces.

According to the experiments of Laufer [17], the fully-developed turbulent flows in boundary layers may be divided into four regimes. These are the viscous sublayer, the layer between the sublayer and the logarithmic layer called the interim layer, the logarithmic layer and the outer region. The spatial ranges of these regimes are $0 \leqslant y \leqslant 5(v/U_\tau)$, $5(v/U_\tau) \leqslant y \leqslant 30(v/U_\tau)$, $30(v/U_\tau) \leqslant y \leqslant 0.2\delta^*$ and $0.2\delta^* \leqslant y$, respectively, where U_τ and δ^* are the friction velocity and the thickness of boundary layer, respectively.

By symmetry, we can restrict our analysis to one-quarter of the square duct. The flow region in the quarter duct can be subdivided into two viscous sublayers, two logarithmic layers (which include the interim layers), a corner region and a center region (see Fig. 2).

The effect of the kinematic viscosity is most dominant within the viscous sublayer, and the turbulent eddy viscosity μ_t may be taken as zero. The flow is computed as a laminar flow with no-slip boundary conditions applied at the wall.
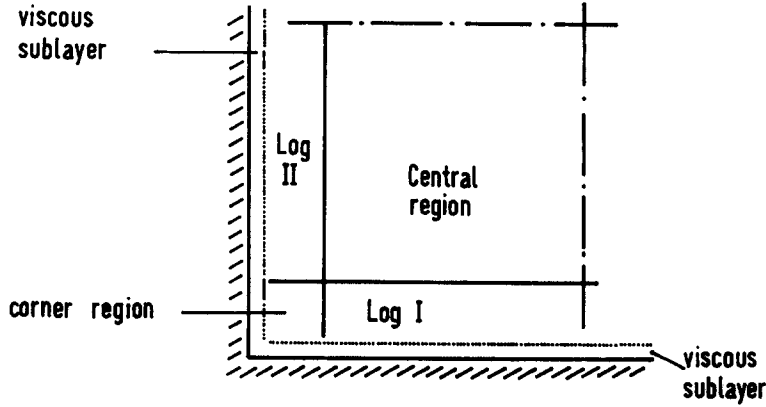
Fig. 2. Sketch of the multi-region of a quarter of the duct.

In the center region, the effect of turbulence takes precedence over the effects of fluid viscosity. It follows that the local flow may be considered as essentially potential, where the viscous damping terms in equations (35) and (36) are made to vanish in this region. The turbulence eddy viscosity is given by equation (23) (i.e. the "far wall" model of Chen and Patel [12]), while the turbulence kinetic energy and rate of dissipation are determined from equations (25) and (26), respectively.

3.1. Logarithmic region

The areas between the center region and the two viscous sublayers, are analogous to the logarithmic layer in a shear flow, henceforth called logarithmic layers I and II to denote the regions near the walls normal to x_2 and x_3, respectively (see Fig. 2). The flow here is characterized by the complex interaction between the wall shear stress and the turbulent kinetic stress. The production of local kinetic energy is assumed to be equal to its dissipation. In logarithmic layer I, for example, we let

$$x_2 = -1 + \delta\eta, \quad \eta = O(1),$$ (40a)

$$U_1 = U_{10} + \delta U_{11} + \cdots, \quad \Omega = \Omega_0/\delta + \Omega_1 + \cdots,$$ (40b)

$$\phi = \delta^2\phi_0 + \cdots \quad \text{and} \quad \psi = \delta\psi_0 + \delta^2\psi_1 + \cdots,$$ (40c)

$$u_{mn} = \delta u_{mn0} + \delta^2 u_{mn1} \cdots, \quad \text{for the pair } mn = 12, 13, 23$$ (40d)

and

$$u_{mn} = u_{mn0} + \delta u_{mn1} + \cdots, \quad \text{for the pair } mn = 22, 23,$$ (40e)

and the governing equations then can be simplified as

$$U_{i0}\frac{\partial U_{10}}{\partial x_i} + U_{20}\frac{\partial U_{10}}{\partial \eta} = -\frac{\overline{dP}}{dx_1} - \frac{\partial u_{120}}{\partial \eta} + \frac{\partial^2}{\partial \eta^2}U_{10}$$ (41)

and

$$U_{i0}\frac{\partial \Omega_0}{\partial x_i} + U_{20}\frac{\partial \Omega_0}{\partial \eta} = \frac{\partial U_{10}}{\partial x_1}\Omega_0 + \frac{\partial U_{30}}{\partial x_1}\frac{\partial U_{10}}{\partial \eta} + \frac{1}{\delta}\left[\frac{\partial^2}{\partial \eta \partial x_3}(u_{330} - u_{220}) + \frac{\partial^2}{\partial \eta \partial \eta}u_{230}\right]$$
$$+ \left[\frac{\partial^2}{\partial \eta \partial x_3}(u_{331} - u_{221}) + \frac{\partial^2}{\partial \eta^2}u_{231}\right] + \frac{\partial^2}{\partial \eta \partial \eta}\Omega_0,$$ (42)

where $i = 1$ or 3 and

$$U_{20} = \frac{\partial \phi_0}{\partial \eta} + \frac{\partial \psi_0}{\partial x_3};$$

$$U_{30} = -\frac{\partial \psi_0}{\partial \eta};$$

and

$$U_{10}\frac{\partial k}{\partial x_1} + U_{20}\frac{\partial k}{\partial \eta} + = \frac{\partial}{\partial \eta}\left[\left(\frac{1}{\sigma_k}C_\mu\frac{k^2}{\epsilon} + \frac{1}{Re}\right)\frac{\partial k}{\partial \eta}\right] + \frac{L_1}{L_2}[P_0 - \epsilon].$$ (43)

The expressions for Reynolds stresses u_{ij0} or u_{ij1} take after

$$u_{120} = -\mu_t \left[\frac{\partial U_{10}}{\partial \eta} \right] \mathrm{Re}, \tag{44a}$$

$$u_{330} - u_{220} = -\frac{2}{C_1} \mu_t \frac{k}{\epsilon} \beta \left[\left(\frac{\partial U_{10}}{\partial x_3} \right)^2 - \left(\frac{\partial U_{10}}{\partial \eta} \right) \mathrm{Re} \right]; \quad u_{331} - u_{221} = -2\mu_t \left[\frac{\partial U_{20}}{\partial \eta} - \frac{\partial U_{30}}{\partial x_3} \right] \tag{44b}$$

and

$$u_{230} = -\frac{2}{C_1} C_\mu \frac{k^3}{\epsilon^2} \beta \left[\left(\frac{\partial U_{10}}{\partial \eta} \frac{\partial U_{10}}{\partial x_3} \right) \right] \mathrm{Re}; \quad u_{231} = 2\mu_t \left[\frac{\partial U_{20}}{\partial x_3} + \frac{\partial U_{30}}{\partial \eta_2} \right], \tag{44c}$$

where the eddy viscosity and the rate of dissipation of turbulent energy are determined by equations (24) and (27), respectively, of the near-wall model.

3.2. Corner region

In the corner region, the flow appears to be the result of a delicate balance between the turbulence dissipation and the induced secondary motion based on balance of the higher order terms. For this reason, we introduce the following scaled transformations:

$$x_2 = -1 + \delta\eta, \quad \eta = O(1); \qquad x_3 = -1 + \delta\xi, \quad \xi = O(1); \tag{45a}$$

and letting

$$U_1 = U_{10} + \delta U_{11} + \cdots; \quad \Omega = \Omega_0 + \delta\Omega_1 + \cdots, \tag{45b}$$

$$\phi = \delta\phi_0 + \cdots \quad \text{and} \quad \psi = \delta\psi_0 + \cdots \tag{45c}$$

and

$$u_{nm} = \delta u_{nm0} + \delta^2 u_{nm1} \ldots, \quad \text{for the pair } mn = 12, 13, 22, 23, 33, \tag{45d}$$

the leading order of the governing equations become

$$U_{10} \frac{\partial U_{10}}{\partial x_1} + U_{20} \frac{\partial U_{10}}{\partial \eta} + U_{30} \frac{\partial U_{10}}{\partial \xi} = -\frac{\overline{\mathrm{d}P}}{\mathrm{d}x_1} - \frac{\partial U_{120}}{\partial \eta} - \frac{\partial u_{130}}{\partial \xi} + \left[\frac{\partial^2}{\partial \eta^2} + \frac{\partial^2}{\partial \xi^2} \right] U_{10}, \tag{46a}$$

$$U_{10} \frac{\partial \Omega_0}{\partial x_1} + U_{20} \frac{\partial \Omega_0}{\partial \eta} + U_{30} \frac{\partial \Omega_0}{\partial \xi} = \frac{\partial U_{10}}{\partial x_1} \Omega_0 - \frac{\partial U_{20}}{\partial x_1} \frac{\partial U_{10}}{\partial \xi} + \frac{\partial U_{30}}{\partial x_1} \frac{\partial U_{10}}{\partial \eta}$$

$$+ \left[\frac{\partial^2}{\partial \xi \, \partial \eta} (u_{330} - u_{220}) + \left(\frac{\partial^2}{\partial \eta \, \partial \eta} - \frac{\partial^2}{\partial \xi \, \partial \xi} \right) u_{230} \right] \Big/ \delta$$

$$+ \left[\frac{\partial^2}{\partial \xi \, \partial \eta} (u_{331} - u_{221}) + \left(\frac{\partial^2}{\partial \eta \, \partial \eta} - \frac{\partial^2}{\partial \xi \, \partial \xi} \right) u_{231} \right]$$

$$+ \left[\frac{\partial^2}{\partial \eta \, \partial \eta} + \frac{\partial^2}{\partial \xi \, \partial \xi} \right] \Omega_0, \tag{46b}$$

$$U_{20} = \frac{\partial \phi_0}{\partial \eta} + \frac{\partial \psi_0}{\partial \zeta}, \quad U_{30} = \frac{\partial \phi_0}{\partial \zeta} - \frac{\partial \psi_0}{\partial \eta} \tag{47}$$

and

$$U_{10} \frac{\partial k}{\partial x_1} + U_{20} \frac{\partial k}{\partial \eta} + U_{30} \frac{\partial k}{\partial \xi} = \frac{\partial}{\partial \eta} \left[\left(\frac{1}{\sigma_k} C_\mu \frac{k^2}{\epsilon} + \frac{1}{\mathrm{Re}} \right) \frac{\partial k}{\partial \eta} \right]$$

$$+ \frac{\partial}{\partial \xi} \left[\left(\frac{1}{\sigma_k} C_\mu \frac{k^2}{\epsilon} + \frac{1}{\mathrm{Re}} \right) \frac{\partial k}{\partial \xi} \right] + L_1 [P_0 - \epsilon]/L_2. \tag{48}$$

With μ_t and ϵ, following equations (24) and (27), we have

$$u_{120} = -\mu_t \left[\frac{\partial U_{10}}{\partial \eta} \right] \text{Re}, \tag{49a}$$

$$u_{130} = -\mu_t \left[\frac{\partial U_{10}}{\partial \zeta} \right] \text{Re}, \tag{49b}$$

$$u_{330} - u_{220} = -\frac{2}{C_1} \mu_t \frac{k}{\epsilon} \beta \left[\left(\frac{\partial U_{10}}{\partial \zeta} \right)^2 - \left(\frac{\partial U_{10}}{\partial \eta} \right)^2 \right] \text{Re}; \quad u_{331} - u_{221} = -2\mu_t \left[\frac{\partial U_{20}}{\partial \eta} - \frac{\partial U_{30}}{\partial \zeta} \right], \tag{49c}$$

$$u_{230} = -\frac{2}{C_1} \mu_t \frac{k}{\epsilon} \beta \left[\left(\frac{\partial U_{10}}{\partial \eta} \frac{\partial U_{10}}{\partial \zeta} \right) \right] \text{Re}; \quad u_{231} = 2\mu_t \left[\frac{\partial U_{20}}{\partial \zeta} + \frac{\partial U_{30}}{\partial \eta} \right]. \tag{49d}$$

The solutions satisfying the equations for the different regions require matching at the interfaces. In the present numerical work, the higher polynomial finite-element method ensures C^1 continuity at each node. This implies continuity (smoothness) in the solutions, its first-order derivatives and mixed second-order derivatives at the interface between the different regions.

4. FINITE-ELEMENT APPROACH AND SOLUTION PROCEDURE

The mathematical model described in Section 3 has four equations of parabolic type [equations (25), (26), (35) and (36)] and two Poisson equations [equations (33) and (34)], for the dependent variable set $\{U_1, \Omega, k, \epsilon, \phi \text{ and } \psi\}$, which may be written as

$$Q_i = [U_1, \Omega, k, \epsilon, \phi, \psi]^T. \tag{50}$$

In general, the governing equations can be reduced to the form

$$U_1 \frac{\partial Q_i}{\partial x_1} + U_L \frac{\partial Q_i}{\partial x_L} = \frac{\partial^2}{\partial x_L} \left(\Gamma_L \frac{Q_i}{\partial x_L} \right) + S_i, \quad Q_i \in D \tag{51a}$$

and

$$L(Q_i) = qQ_i + r \frac{\partial}{\partial x_L} Q_i \cdot \mathbf{n} + s = 0, \quad Q_i \in \partial D. \tag{51b}$$

The Poisson-type equations may be treated as a special case of equation (51a). Here $i = 1, 2, 3$ and $L = 2, 3$; S_i represent the source terms corresponding to equations (25), (26) and (33)–(36); q, r and s are specified coefficients and $\mathbf{n}$ is the outward unit normal vector. The solution domain of equation (51a) is $D(\equiv \mathbb{R}^2 \times [x_1(0), x_1])$ and its boundary is $\partial D[\equiv \partial \mathbb{R}^2 \times [x_1(0), x_1])$. To start the calculation, an initial distribution for Q_i on $D_0(= \mathbb{R}^2 \times x_1(0))$ is required.

The Galerkin finite-element approach is to find $Q_i^h \in H_0^1(D)$, which satisfies the equation

$$a(Q_i^h, U_1^h, N_k) + b(Q_i^h, U_L^h, N_k) = c(Q_i^h, N_k) + e(Q_i^h, N_k), \quad \forall N_k \in H_0^1(D), \tag{52}$$

where

$$a(Q_i^h, U_1^h, N_k) = \int_D N_k U_1 \frac{\partial Q_i^h}{\partial x_1} \, \mathrm{d}x_L, \tag{53a}$$

$$b(Q_i^h, U_L^h, N_k) = \int_D N_k U_L^h \frac{\partial Q_i^h}{\partial x_L} \, \mathrm{d}x_L, \tag{53b}$$

$$c(Q_i^h, N_k) = \int_D \frac{\partial N_k}{\partial x_L} \Gamma_L \frac{\partial Q_i^h}{\partial x_L} + N_k [S_p Q_i^h + S_p] \, \mathrm{d}x_L, \tag{53c}$$

$$e(Q_i^h, N_k) = \oint_{\partial D} N_k L(Q_i^h) \, \mathrm{d}\sigma \tag{53d}$$

and

$$U_2^h = \frac{\partial \phi^h}{\partial x_2} + \frac{\partial \phi^h}{\partial x_3} \quad \text{and} \quad U_3^h = \frac{\partial \phi^h}{\partial x_3} - \frac{\partial \psi^h}{\partial x_2}. \tag{54}$$

Here $[N_k(x_L)]^T$ is a row matrix whose elements are polynomials on x_L ($L = 2, 3$) constructed to form a cardinal basis, $d\sigma$ is the line integral element, $H_0^1(D)$ denotes the Hibert space of all functions possessing square integrable first derivatives and satisfying the boundary conditions (51b). In the present work, rectangular elements utilizing bicubic Hermite polynomials are used and the integral in equation (52) is carried out using a Gauss routine based on 5×5 Gaussian points. For a typical 100-element representation in a quarter-square duct, 1 layer of elements is used for the viscous sublayer $(x_2', x_3' \leqslant 5(v/U_t))$, 3 layers of elements are used for the logarithmic region $(5(v/U_t) \leqslant x_2', x_3' \leqslant 0.2D_h)$ and 16 elements are used to represent the corner region (see Section 3 and Fig. 2). After the respective matrices are assembled, a direct-banded matrix solver is employed for matrix inversion. For other details about the finite-element solution procedure, the reader is referred to Brooks and Hughes [18].

Those differential equations introduced above which are parabolic in the streamwise direction imply that influence is only permitted in the downstream direction. An efficient forward-marching, finite-difference procedure can thus be employed for numerical integration downstream.

For the initial conditions, the numerical solution of steady-state laminar flow in a square duct was used for the streamwise velocity, while the functions Ω, ψ and ϕ took on null values. The distributions of the turbulence quantities k and ϵ were established using the standard wall function approach.

Boundary conditions are specified as follows. Along the plane of symmetry of the square duct, the velocity component normal to the surface was set equal to zero, while for the quantities k and ϵ, the gradients normal to the surface were taken as zero; thereupon, the quantities Ω, the normal gradient of ϕ and the tangential gradient of ψ had to be set to zero on this surface. Along the solid walls, the velocity components and Reynolds stresses are set equal to zero. The normal gradient of ϕ and the tangential gradient of ψ assume null values along the walls. The axial vorticity is hence evaluated from equation (34).

The forward-marching step size is set to 0.01 of the duct hydraulic diameter D_h. Since the initialization for turbulent quantities was inaccurate, integration was first carried out to the location $x_1'/D_h = 5$, solving only for U_1, k and ϵ, with the assumption of a Boussinesq eddy viscosity. With these data as Q_i^0 (which are U_1, k or ϵ), the streamwise velocity U_1, followed by Ω, k and ϵ, and finally ψ and ϕ, were solved for subsequent downstream values.

Evolution of the flow in a square duct was calculated for $Re = 50,000$, $65,000$ and $250,000$ until a fully-developed state was reached. In all our computations, the fully-developed state occurred at a downstream location of $x_1'/D_h \geqslant 80$. The accuracy of the computations was checked using different element sizes. It was found that the solutions obtained with a different number of elements,
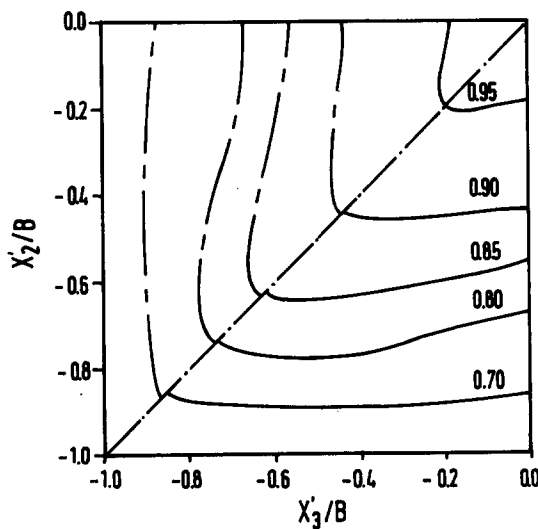

Fig. 3. Contours of the primary velocity U_1'/U_b: ——, experimental measurements of Melling and Whitelaw [19], $Re = 42,000$; – – –, present computation $Re = 50,000$.
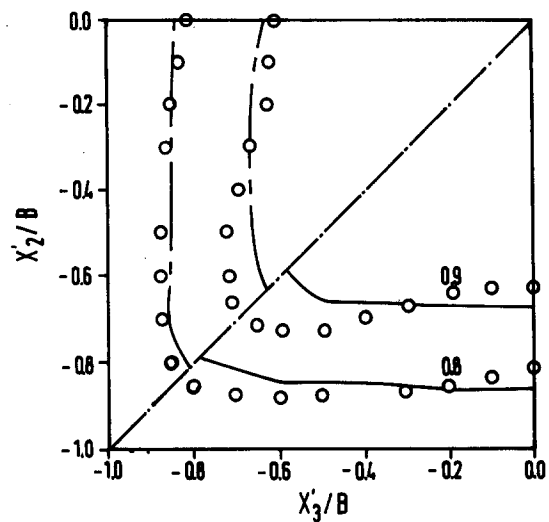
Fig. 4. Contours of the primary velocity (U_1'/U_{1max}) for $Re = 250,000$: $\bigcirc$, experimental measurements of Gessner and Emery [6]; ——, prediction by D&R [11]; – – –, present prediction.

notably 64, 81 and 100, agreed well and consistently with each other. With 64 elements, a typical run to steady-state took about 280 min of CPU time on the NEC SX-1A supercomputer.

5. RESULTS AND DISCUSSION

5.1. Comparison with other experimental and numerical results

The contours of the streamwise velocity distribution for fully-developed flow are shown in Figs 3 and 4 for Re = 50,000 and 250,000, respectively. The present calculation is in good agreement with the experimental measurements of Melling and Whitelaw [19] at $x_1'/D_h = 36.8$ for different primary velocity quantities, with U_1'/U_b varying from 0.7 to 0.95 (Fig. 3). [It should be noted that judging from the numerical works by Demuren and Rodi [11], hereafter abbreviated to D&R (subsequently shown in Fig. 7), and Myong and Kobayashi [14, 15] (not shown), which indicate relatively little variation in the secondary velocity profiles at $x_1'/D_h = 40$ and 84, they suggest that the data of Melling and Whitelaw [19] at $x_1'/D_h = 36.8$ is asymptotically close to the fully-developed state for comparison.] In Fig. 4, two contours of primary velocity evaluated ($U_1'/U_{1max} = 0.8$, 0.9) by the present model compare favorably with the experimental data of Gessner and Emery [6] at $x_1'/D_h = 84$ for Re = 250,000. In fact, our numerical prediction, on comparison with the D&R calculation, shows increased bulging of the velocity contours towards the corner and agrees better with the experimental data. As can be seen subsequently in Fig. 7, underprediction of the secondary motion in the D&R scheme has resulted in the less-pronounced bulging of the isovels.

The secondary flow velocity vector distribution for Re = 65,000 is shown in Fig. 5. The experimental data of Fujita et al. [20] are replotted in Fig. 5(b). Apart from the slight asymmetry detected in the experimental measurements, both plots show the existence of a pair of contrarotating longitudinal vortices in each quadrant of the square-duct cross-section.

Evolution of the secondary flow is shown in Fig. 6, where the stream function of secondary motion for Re = 50,000 is plotted at different downstream locations. These plots should not be taken in the strict literal sense of the actual distance downstream of the inlet for comparison with experimental results, since the computed flow was not initiated with uniform flow as at the entrance of the duct. It is not the intention of this work to track the full developing flow field, but to see how the secondary flow features evolve under the influence of turbulent shear stresses. Near the entrance section (where all variables are solved), small values of the cross-plane stream function ψ first appear in the region close to the corner [Fig. 6(a)]. As the flow progresses downstream, the magnitude of ψ increases and the results imply the existence of a pair of axial vortices rotating in opposite directions to each other [Fig. 6(b)]. With further distance downstream, the vortical pair
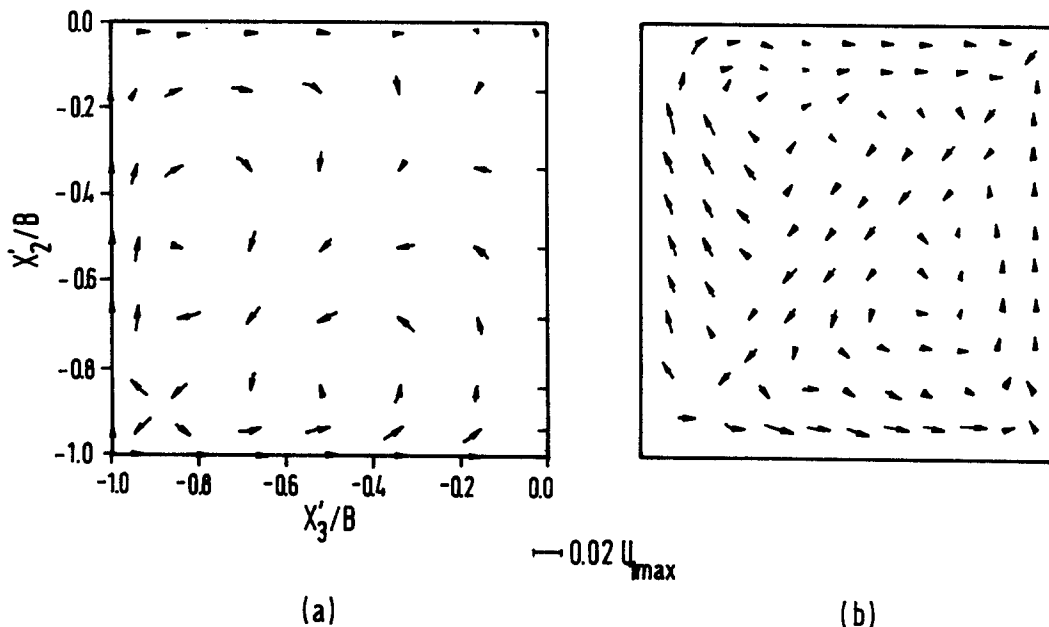

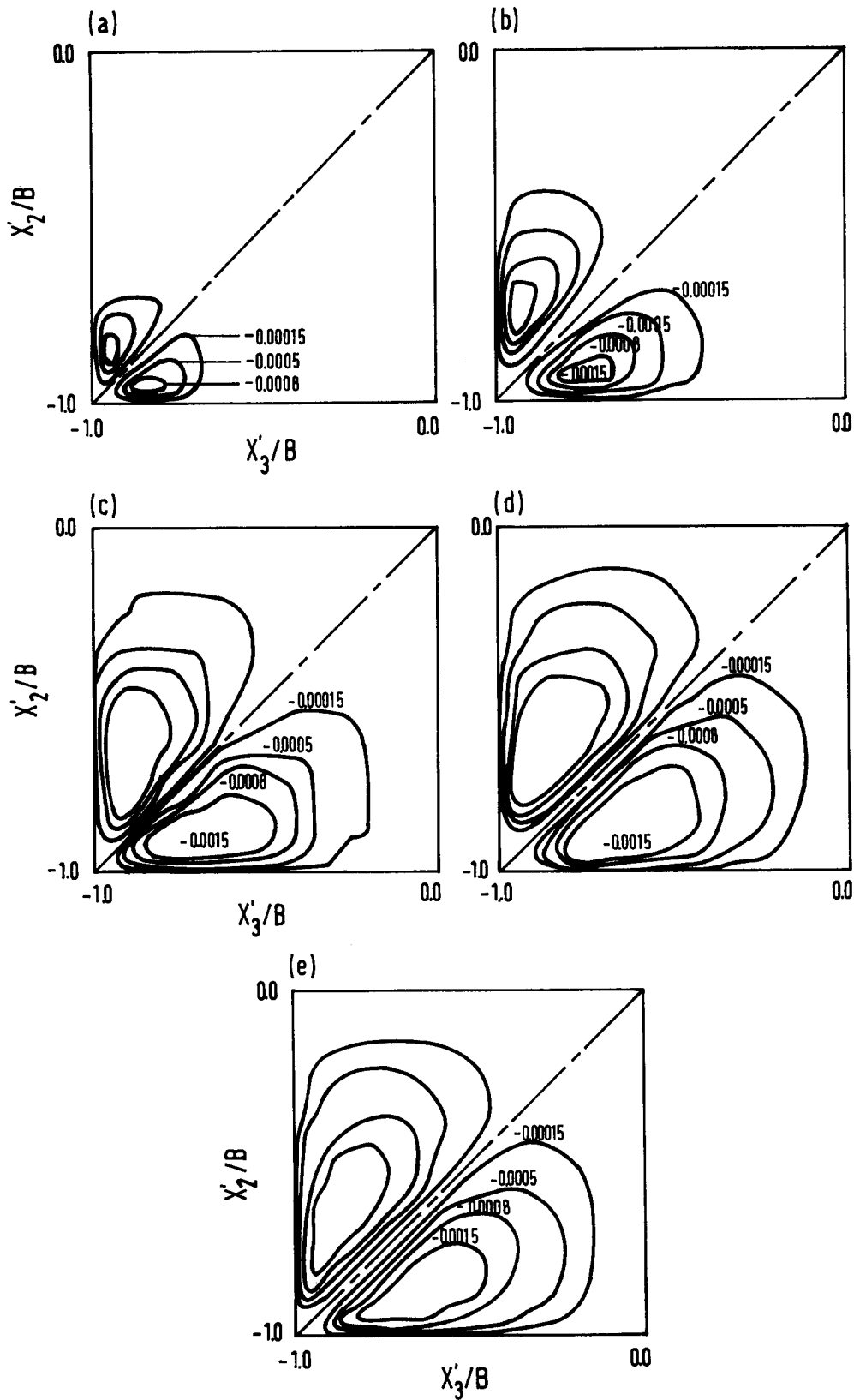Fig. 5. Secondary flow vectors: (a) present prediction; (b) experimental results of Fujita et al. [20].

Fig. 6. Contours of the stream function ψ at the different streamwise locations, Re = 50,000: (a) $x_1' = 9D_h$; (b) $x_1' = 18D_h$; (c) $x_1' = 28D_h$; (d) $x_1' = 42D_h$; (e) $x_1' = 86D_h$.

diffuses outward and the vortex centers, originally located near the corner, move toward the center region [as depicted in Fig. 6(c,d)] until a fully-developed state is obtained [Fig. 6(e)]. Figure 6 shows that the stream function ψ takes on quantities equal in value but opposite in sign in the respective "upper-diagonal" and "lower-diagonal" portions. Our results have indicated that the secondary motion originates in the region near the corner for a developing flow. The predictions of Gessner and Emery [6] have shown that the magnitude (scale) of this motion can be sensitive to grid-spacing effects if the grid in the cross-plane is not sufficiently fine. Other numerical studies, including the recent work of Myong and Kobayashi [14, 15] who used an anisotropic k–ϵ modeling of the turbulence quantities, have found that the secondary flow originates near the corner in the entrance region. These computed results appear to be supported by the experimental evidence of Ahmed and Brundrett [21].

Comparisons of secondary velocity profiles by the present model with the D&R scheme are shown in Fig. 7 for streamwise locations of $x'_1 = 40D_h$ and $84D_h$. The experimental data of Gessner and Emery [6] are also included. Figure 7(a) shows the abscissa taken along the wall bisector with varying x_2 coordinate. Our results tend to underpredict the maximum secondary velocity in
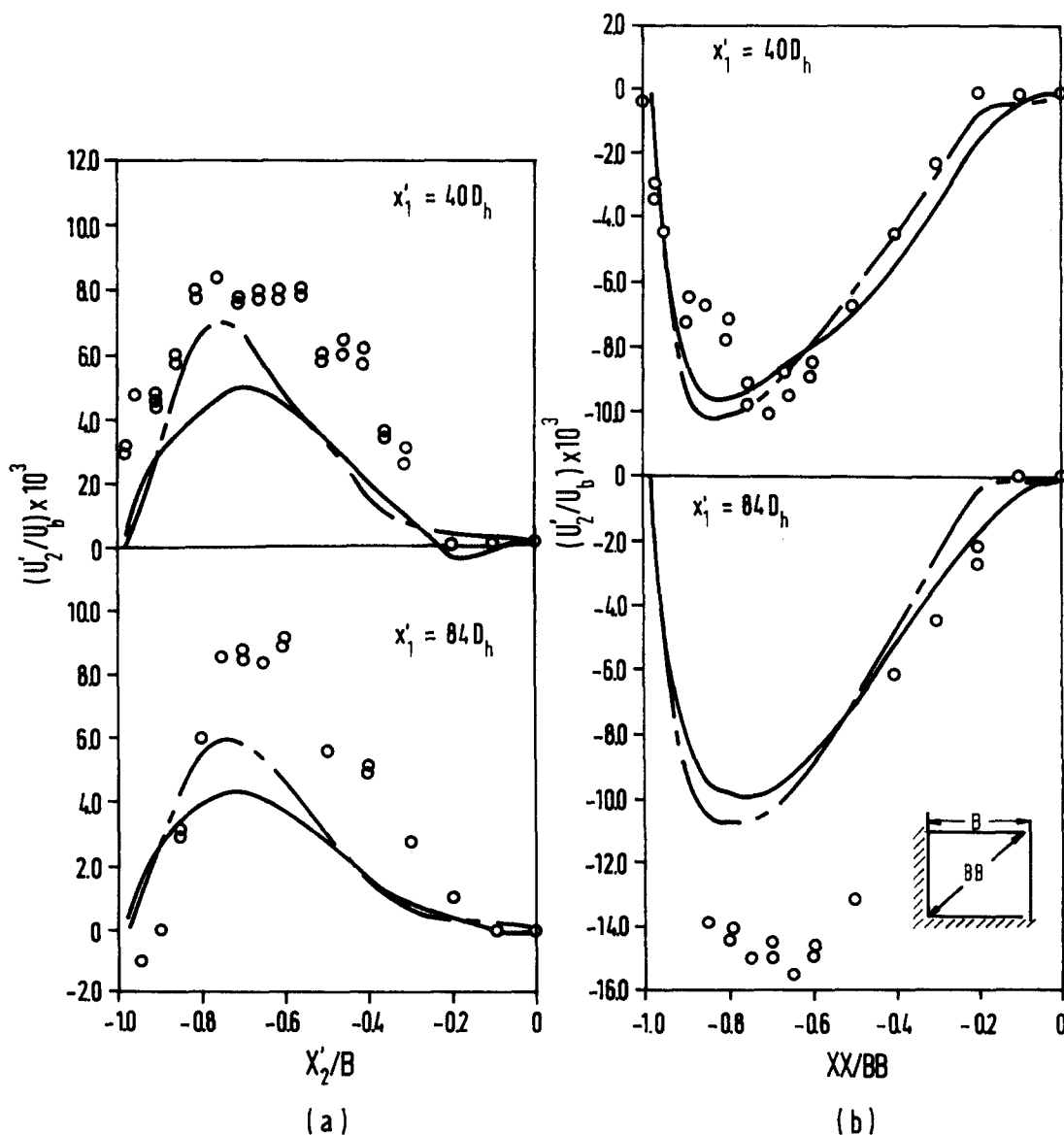

Fig. 7. Secondary velocity profiles for $Re = 250,000$ along the (a) wall and (b) corner bisector: O, experimental measurements of Gessner and Emery [6]; ———, prediction by D&R [11]; — — —, present prediction.
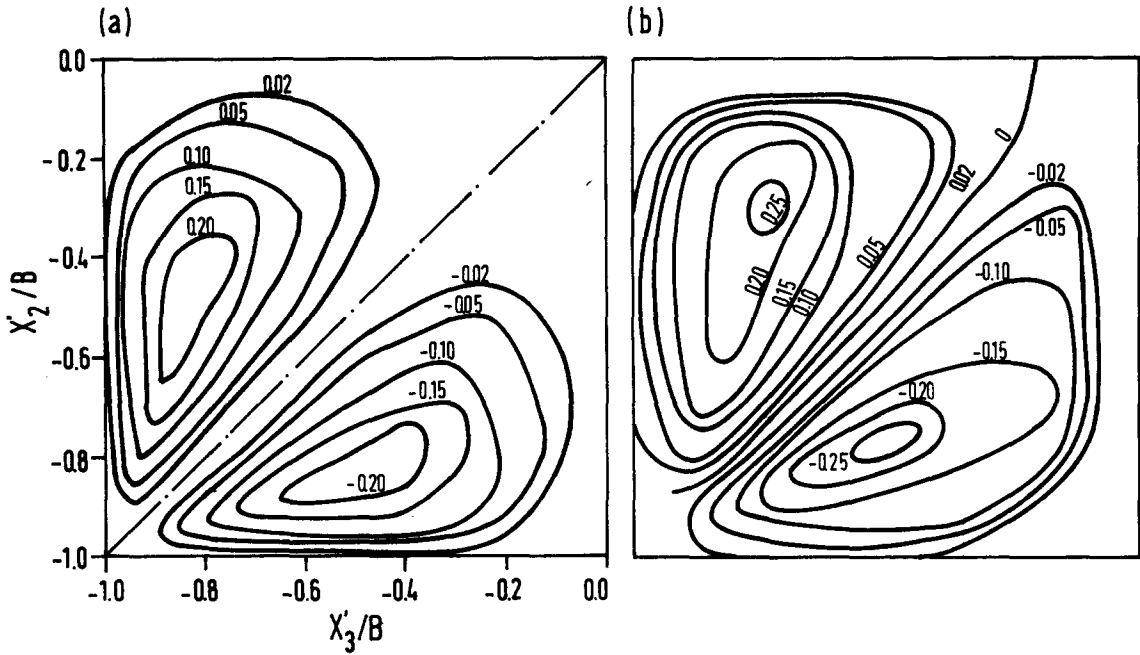
Fig. 8. Contours of the fully-developed axial vorticity $(\Omega' D_h / U_{1max})$ for Re = 65,000: (a) present prediction; (b) experimental measurements of Yokosawa et al. [22].

comparison with the experimental data. However, our underprediction is significantly less than the predictions of the D&R scheme, especially at a streamwise location of $x'_1 = 40D_h$. In Fig. 7(b), where the abscissa is taken to be the corner bisector, at a streamwise location of $x'_1 = 40D_h$ agreement with the experimental data is better. However, at $x'_1 = 84D_h$, both our simulation and the D&R model underpredict the secondary velocity by a fairly large margin. (This is also the case for the numerical work by Myong and Kobayashi [14, 15] (not shown), where there is a significant underprediction at $x'_1 = 84D_h$ along both the wall and corner bisectors.) Overall, there is no major difference between the two models except that our simulation shows slightly better agreement with the peak secondary velocity, more so along the corner bisector.

In Fig. 8 contours of fully-developed axial vorticity $\Omega' D_h / U_{1max}$ for Re = 65,000 are shown (here Ω' is the dimensional value of Ω). The experimental results by Yokosawa et al. [22] are included for comparison. There is fair agreement between the two plots in the distribution and magnitude of the contours. It should be noted that inherent experimental errors associated with the measurement of velocity gradients and the use of a hot-wire anemometer, which necessarily induces disturbances to the flow field, probably account for the apparent asymmetry seen in the vorticity contour plot of Fig. 8(b).

Figure 9 shows distributions of the lateral component of the Reynolds shear stress $\overline{u'_1 u'_3}/U_b^2$ (or $\overline{u'_1 u'_2}/U_b^2$) at Re = 65,000. Unlike other figures, the contours of $\overline{u'_1 u'_3}/U_b^2$ (or $\overline{u'_1 u'_2}/U_b^2$) are only symmetric about the wall bisector of a square duct. Our computed results bear fair resemblance to the experimental data of Yokosawa et al. [22]. Disagreement of the results is most pronounced in the center region of the duct, since we have effectively assumed potential flow with the kinematic viscosity set equal to zero in our computation. Despite this, the general distribution of the contour lines and magnitudes are deemed reasonable when compared with the experiments. There is a conspicuous absence of data close to the wall region, which is probably due to both the difficulties of measurement and the strong wall effect on the accuracy of measurement.

Figure 10 depicts the corresponding transverse Reynolds stress difference $(\overline{u'_3 u'_3} - \overline{u'_2 u'_2})/U_b^2$ with the experimental measurements of Fujita et al. [20]. Other than the apparent asymmetry seen in the experimental data of Fig. 10(b) (which can be attributed to the uncertainty and difficulty in physically measuring small differences in the Reynolds stresses), the numerical data concur quite well with the former. Near the wall, the magnitudes of our computed contours are about equal to the experimental contours and their distribution shows the right trend.
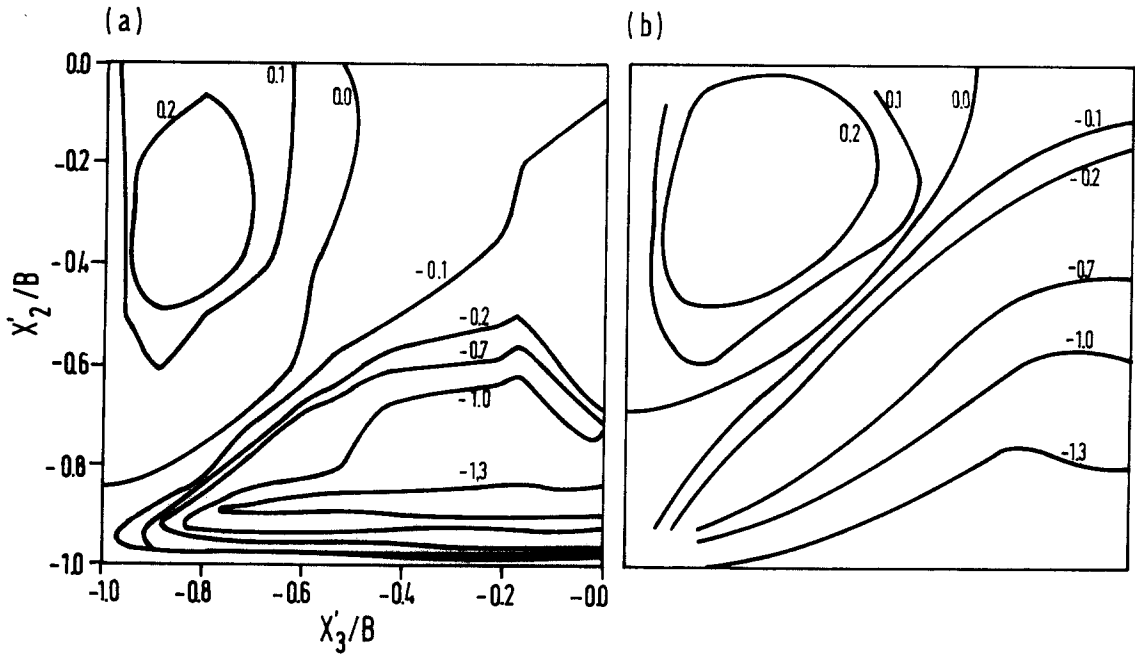
Fig. 9. Contours of the lateral Reynolds shear stress $(\overline{u_1'u_3'}/U_b^2) \times 10^3$ for Re = 65,000: (a) present prediction; (b) experimental measurements of Yokosawa et al. [22].

In Fig. 11 we show the distribution of turbulent kinetic energy along the wall bisector (a) and along the corner bisector (b). Shown together are the experimental data taken from Gessner and Emery [6] at Re = 250,000. In Fig. 11(a), the distribution is in excellent agreement with the experiments, except near the wall. For Fig. 11(b), near the corner region, our calculation overpredicts k. In other regions, our distributions of k concur rather well with the experimental results and the numerical predictions by the D&R model.

In our work, since the no-slip boundary condition at the wall is used in place of the common wall function specification, the wall shear stress and its distribution can be evaluated directly from
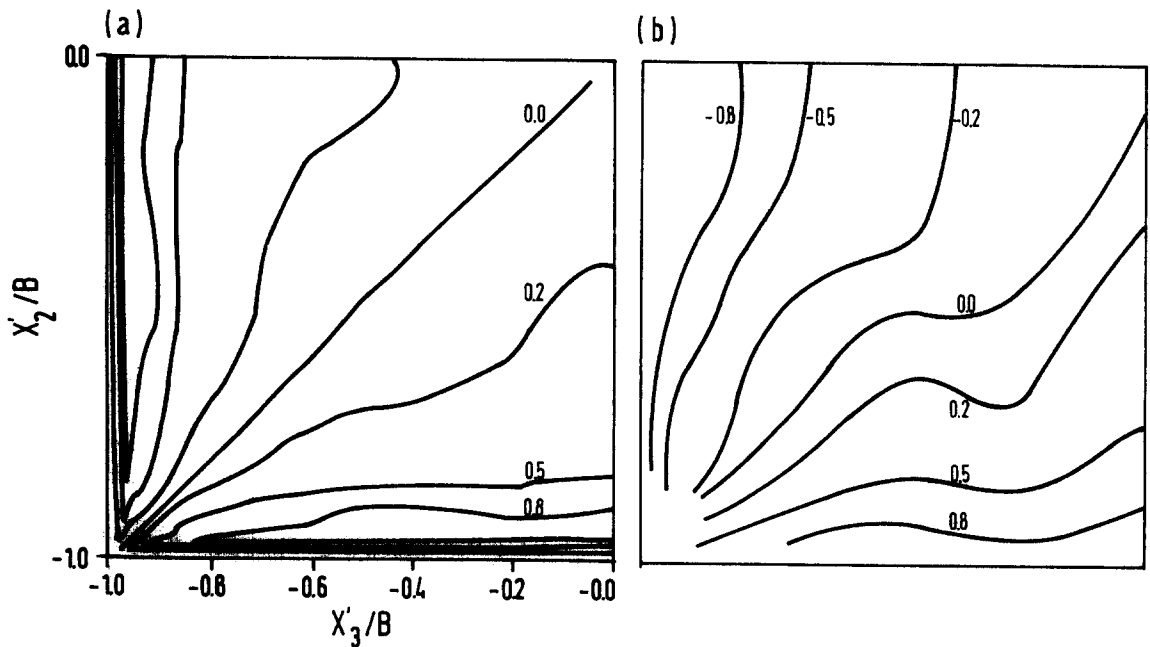

Fig. 10. Contours of the transverse Reynolds shear stress $(\overline{u_3'u_3'} - \overline{u_2'u_2'})/U_b^2) \times 10^3$ for Re = 65,000: (a) present prediction; (b) experimental measurements of Fujita et al. [20].
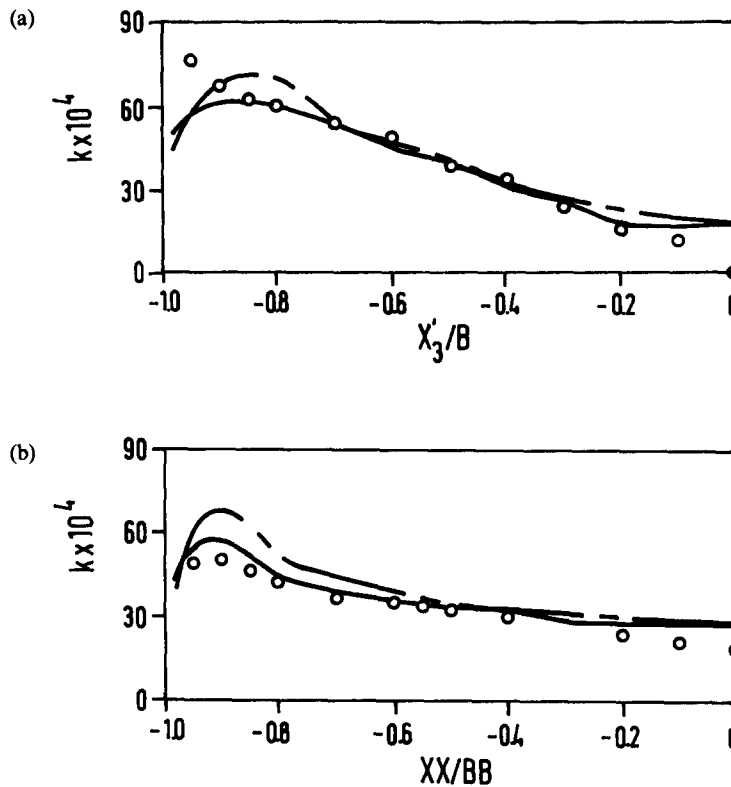
Fig. 11. Turbulent kinetic energy profiles for Re = 250,000: O, experimental measurements of Gessner and Emery [6]; ————, prediction by D&R [11]; ————, present prediction. (a) Wall bisector; (b) corner bisector.

the streamwise velocity gradient at the wall. The fully-developed flow (mean) skin friction coefficient, C_f, calculated at Re = 50,000, 65,000 and 250,000, yields numerical values of 0.005155, 0.004787 and 0.003710, respectively. These quantities compare vary favorably with the computed results of Myong [13] which, in turn, agree well with the experimental values reported in Refs [6, 23–25]. Figure 12 shows the distribution of the local wall shear stress (non-dimensionalized w.r.t. the mean shear stress) for fully-developed flow, which is compared with the experimental data of Yokosawa et al. [22] and Gessner and Emery [6] for Re = 650,000 and 250,000, respectively. Plotted also is the numerical prediction of Myong [13]. The agreement of our results with both experimental and numerical data is excellent, with the wall shear stress increasing in magnitude from the value at the wall bisector towards the corner, and eventually decreasing towards zero right at the corner. It can also be seen that the effect of the Re on the shape of distribution is not very significant.

5.2. Origin of the secondary flow

In the literature, there is some disagreement on the origin and generation of the secondary flows. The contribution of the anisotropy of cross-plane normal stress has been considered to be of special importance for the generation of secondary flow by some authors, like Brundrett and Baines [3] who carried out measurements on the six Reynolds stress components in fully-developed square-duct flow. This view was further supported by Yokosawa et al. [22] in their experiments. Another school of thought [4, 26] suggested that the turbulent normal and shear stress terms, as they appear in equation (39), are of the same order and opposite in sign based on their experimental results. Perkins [26] considered that two different mechanisms are responsible for the likely source of secondary shear stress. One mechanism is the gradient of secondary velocities, and the other mechanism is associated with the distortion of the primary stress field in the corner, as deduced from the primary velocity gradients. Still, Gessner [27] claimed that it is not the anisotropy of the turbulent normal stresses that play a major role for the generation of secondary motion, but the transverse gradients of the primary shear stresses in the corner region. Finally D&R, after reviewing
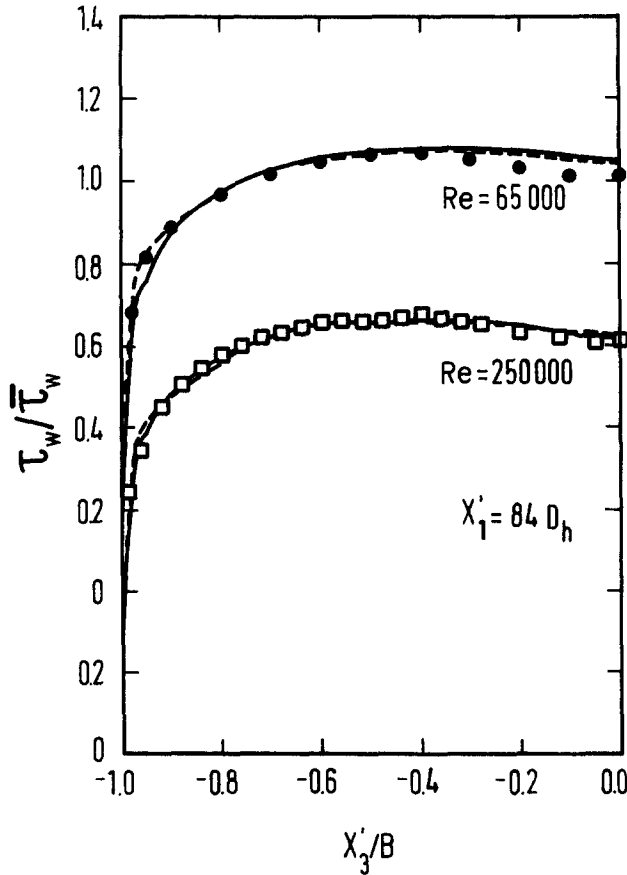
Fig. 12. Local wall shear stress distributions for fully-developed flow: □, experimental measurements of Gessner and Emery [6]; — — —, experimental measurements of Yokosawa et al. [22]; ————, prediction by Myong [13]; — — —, present prediction.

the available experimental data, stated that gradients of normal and tangential stresses in the cross-plane are of much larger order than the convective and viscous terms in the streamwise vorticity equation, and it is their small difference (having the same order of magnitude as the convective terms) that drives the secondary motion.

In our work, the analysis of Section 2, using an order-of-magnitude and power-series expansion resulting in equation (39), clearly supports the conclusion reached by D&R that the difference in the second-order gradients of the normal and transverse Reynolds stresses provide the main driving force for the secondary motion. In order to check this conclusion, two separate computations were made. In one run, all the terms pertaining to the right-hand side of equation (36) were evaluated. In a separate case, equation (36) was replaced by equations (38) and (39).

Figure 13 depicts gradients of the normal Reynolds stresses $\partial^2(u_{33} - u_{22})/\partial x_2 \partial x_3$ and transverse Reynolds stresses $-[(\partial^2/\partial x_3 \partial x_3) - (\partial^2/\partial x_2 \partial x_2)]u_{23}$, which are found to be comparable in magnitude but opposite in sign. The difference between these two terms, denoted by $\Delta\zeta$, is shown concurrently on an ordinate scale magnified 10 times to depict the fine distribution. The figure distinctly shows that the secondary order of $\Delta\zeta$ (denoted by $\Delta\zeta_2$) obtained with the leading order of $\Delta\zeta$ (denoted by $\Delta\zeta_1$) set equal to zero, follows the distribution of the full $\Delta\zeta$ rather well along different planes of x_2'/B. At $x_2'/B = -0.98$ (i.e. very close to the wall), $\Delta\zeta_2$ is almost identical to $\Delta\zeta$, except for the peak and trough of the respective $\Delta\zeta$ and $\Delta\zeta_2$ distributions which differ slightly more. For $x_2'/B = -0.92$, the difference between $\Delta\zeta$ and $\Delta\zeta_2$ is negligible, while at $x_2'/B = -0.84$ the difference is only more pronounced for locations away from the duct corner. Overall, these three plots suggest that the source of the secondary motion in a duct lies in the second-order term of $\Delta\zeta$ which provides the essential driving force for the convection and diffusion of the vorticity term Ω. These computed results reinforce our earlier analysis using expansion of the appropriate terms in Section 2.4, culminating in equation (39).

6. CONCLUDING SUMMARY

By using an order-of-magnitude analysis with the vector-potential function formulation, we have been able to reduce the governing equations for turbulent flow in a square duct to a set of four parabolic and two Poisson equations. In turbulence modeling, the algebraic Reynolds stress model of Demuren and Rodi [11] combined with the two-layer approach of Chen and Patel [12] for turbulence viscosity has enabled the specification of no-slip boundary conditions at the wall in place of the commonly used wall functions. Together with the division of the flow domain into various regions to reflect localized physical phenomena, the resulting equations are numerically integrated using a finite-element representation in each cross-sectional plane with finite-difference marching in the streamwise direction. Such a combination of schemes is chosen to facilitate the future study of continuously changing cross-sectional shape in the streamwise direction, seen in most jet-engine inlet configurations. The present results obtained for flow in a square-duct section compare well with the available experimental results for both primary and secondary flow quantities. The results are also in good agreement with other numerical works, like Demuren and Rodi [11] and Myong and Kobayashi [14, 15].
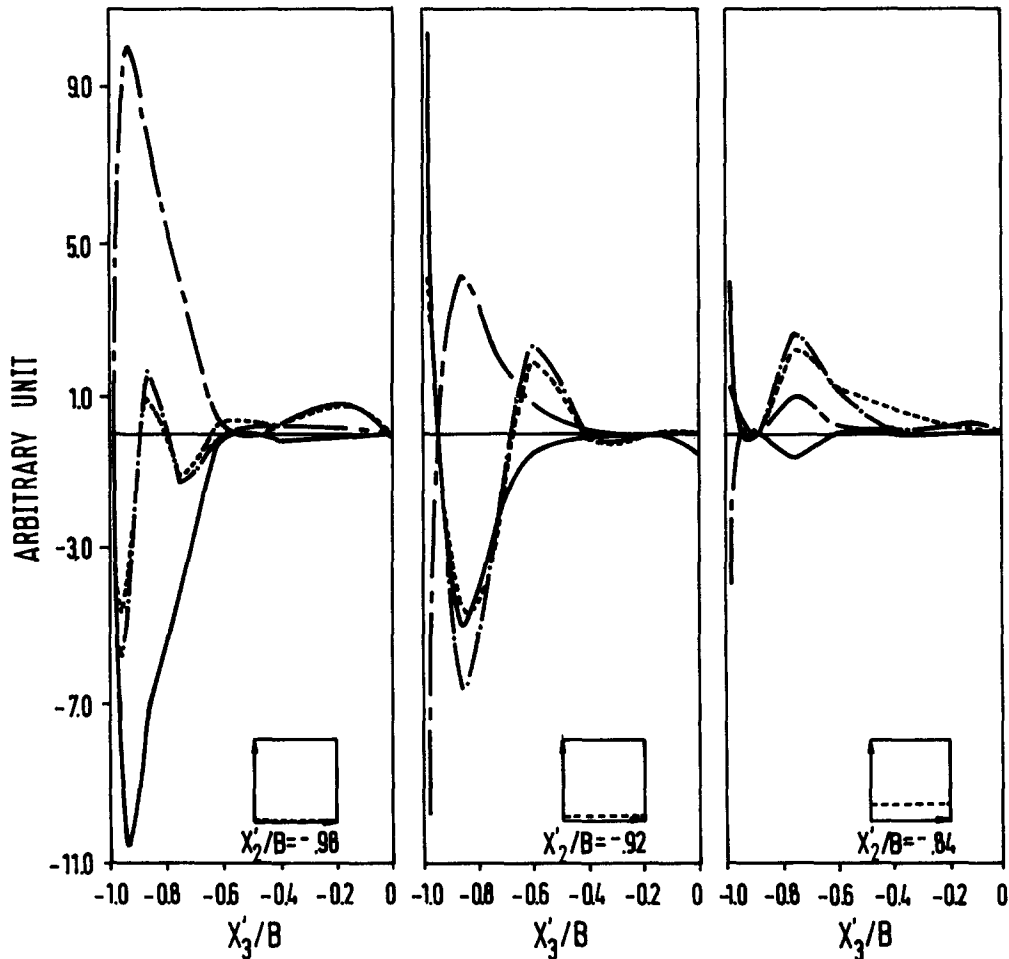

Fig. 13. Gradients of Reynolds normal stress and transverse shear stress terms as they appear in the axial vorticity equation (36) Re = 65,000:

$$\frac{\partial^2}{\partial x_2 \partial x_3}(u_{33} - u_{22}); \quad -\left(\frac{\partial^2}{\partial x_3 \partial x_3} - \frac{\partial^2}{\partial x_2 \partial x_2}\right)u_{23};$$

$$10 \times \left\{\frac{\partial^2}{\partial x_2 \partial x_3}(u_{33} - u_{22}) - \left(\frac{\partial^2}{\partial x_3 \partial x_3} - \frac{\partial^2}{\partial x_2 \partial x_2}\right)u_{23} \equiv \Delta\zeta\right\};$$

$$10 \times \left\{\frac{\partial^2}{\partial x_2 \partial x_3}(u_{331} - u_{221}) - \left(\frac{\partial^2}{\partial x_3 \partial x_3} - \frac{\partial^2}{\partial x_2 \partial x_2}\right)u_{231} \equiv \Delta\zeta_2\right\}.$$

An important outcome of expanding terms of interest to different orders (Section 2.4) is the interpretation analytically that the origin of secondary motion in a duct can be largely attributed to the second-order terms of the difference in the gradients of the normal and transverse Reynolds stresses. This conclusion differs considerably from the view of Yokosawa et al. [22], who considered the cross-planar normal stresses to be the major cause of the secondary motion, and supports the conclusion reached by Demuren and Rodi [11].

REFERENCES

1. J. Nikuradse, Turbulente strömung in nicht-kreisförmigen rohren. *Ing. Arch.* **1**, 306 (1930).
2. L. C. Hoagland, Fully developed turbulent flow in straight rectangular ducts-secondary flow, its cause and effect on the primary flow. Ph.D. Thesis, MIT, Cambridge, MA (1960).
3. E. Brundrett and W. D. Baines, The production and diffusion of vorticity in duct flow. *J. Fluid Mech.* **19**, 375 (1964).
4. F. B. Gessner and J. B. Jones, On some aspects of fully developed turbulent flow in a rectangular channel. *J. Fluid Mech.* **23**, 689 (1965).
5. B. E. Launder and M. M. Ying, Secondary flows in ducts of square cross-section. *J. Fluid Mech.* **54**, 289 (1972).
6. F. B. Gessner and A. F. Emery, The numerical prediction of developing turbulent flow in rectangular ducts. *Trans. ASME Jl Fluids Engng* **103**, 445 (1981).
7. A. A. M. Aly, A. C. Trupp and A. D. Gerrard, Measurements and prediction of fully developed turbulent flow in an equilateral triangular duct. *J. Fluid Mech.* **85**, 57 (1978).
8. V. Ramachandra, The numerical prediction of flow and heat transfer in rod-bundle geometries. Ph.D. Thesis, Univ. of London (1979).
9. D. D. Gosman and C. W. Rapley, A prediction method for fully developed flow through non-circular passages. In *Numerical Method in Laminar and Turbulent Flows* (Edited by C. Taylor *et al.*). Pineridge Press, Swansea, U.K. (1978).
10. S. V. Patankar and D. B. Spalding, A calculation procedure for heat, mass and momentum transfer in three-dimensional parabolic flows. *Int. J. Heat Mass Transfer* **15**, 1787 (1972).
11. A. O. Demuren and W. Rodi, Calculation of turbulence-driven secondary motion in non-circular ducts. *J. Fluid Mech.* **140**, 189 (1984).
12. H. C. Chen and V. C. Patel, Practical near-wall turbulence models for complex flows including separation. *AIAA Jl* **26**, 641 (1988).
13. H. K. Myong, Numerical investigation of fully developed turbulent flow and heat transfer in a square duct. *Int. J. Heat Fluid Flow* **12**, 344 (1991).
14. H. K. Myong and T. Kobayashi, Numerical simulation of three-dimensional developing turbulent flows in a square duct with the anisotropic $k-\epsilon$ model. In *Advances in Numerical Simulation of Turbulent Flows; ASME FED* **117**, 17. ASME, New York (1991).
15. H. K. Myong and T. Kobayashi, Prediction of three-dimensional turbulent flow in a square duct with an anisotropic low Reynolds number $k-\epsilon$ model. *Trans. ASME Jl Fluids Engng* **113**, 608 (1991).
16. B. E. Launder, G. Reece and W. Rodi, Progress in the development of a Reynolds stress turbulent closure. *J. Fluid Mech.* **68**, 537 (1975).
17. J. Laufer, Investigation of turbulent flow in a two-dimensional channel. NASA Report 1053 (1951).
18. A. N. Brooks and T. Hughes, Streamline upwind/Petrov–Galerkin formulation for convection dominated flows with particular emphasis on the incompressible Navier–Stokes equations. *Computer Meth. Appl. Mech. Engng* **32**, 199 (1982).
19. A. Melling and J. H. Whitelaw, Turbulent flow in a rectangular duct. *J. Fluid Mech.* **78**, 289 (1976).
20. H. Fujita, H. Yokosawa and M. Hirota, Secondary flow of the second kind in rectangular ducts with one rough wall. *Expl Therm. Fluid Sci.* **2**, 72 (1989).
21. S. Ahmed and E. Brundrett, Turbulent flow in non-circular ducts. Mean flow properties in the developing region of a square duct. *Int. J. Heat Mass Transfer* **14**, 365 (1971).
22. H. Yokosawa, H. Fujita, M. Hirota and S. Iwata, Measurement of turbulent flow in a square duct with roughened walls on two opposite sides. *Int. J. Heat Fluid Flow* **10**, 125 (1989).
23. J. P. Hartnett, J. C. Y. Koh and S. T. A. McComas, A comparison of predicted and measured friction factors for turbulent flow through rectangular ducts. *Trans. ASME J. Heat Transfer* **84**, 82 (1962).
24. H. J. Leutheusser, Turbulent flow in rectangular ducts. *J. Hydraul. Div. Proc. ASCE* **89**(HY3), 1 (1963).
25. E. G. Lund, Mean flow and turbulence characteristics in the near corner region of a square duct. M.Sc. Thesis, Univ. of Washington, Seattle, WA (1977).
26. H. J. Perkins, The formation of streamwise vorticity in turbulent flow. *J. Fluid Mech.* **44**, 721 (1970).
27. F. B. Gessner, The origin of secondary flow in turbulent flow along a corner. *J. Fluid Mech.* **58**, 1 (1973).